COMMUNICATIONS IN COMPUTATIONAL PHYSICS
Vol. **4**, No. 4, pp. 838-859

Commun. Comput. Phys.
October 2008

Electrostatic-Aerodynamic Compression in Hypersonic Cylindrical Inlet

J. S. Shang*

Department of Mechanics and Materials Engineering, Wright State University, Dayton, OH 45435, USA.

Received 20 June 2007; Accepted (in revised version) 18 October 2007

Communicated by Jan S. Hesthaven

Available online 28 May 2008

Abstract. Hypersonic magneto-fluid-dynamic interaction has been successfully performed as a virtual leading-edge strake and a virtual cowl of a rectangular inlet. In a side-by-side experimental and computational study, the magnitude of the induced compression was found to depend on configuration and electrode placement. To better understand the interacting phenomenon the present investigation is focused on a direct current discharge at the leading edge of a cylindrical inlet for which validating experimental data is available. The present computational result is obtained by solving the magneto-fluid-dynamics equations at the low magnetic Reynolds number limit and using a nonequilibrium weakly ionized gas model based on the drift-diffusion theory. The numerical simulation provides a detailed description of the intriguing physics. After validation with experimental measurements, the computed results further quantify the effectiveness of a magneto-fluid-dynamic compression for a hypersonic cylindrical inlet. A minuscule power input to a direct current surface discharge of 8.14 watts per square centimeter of electrode area produces an additional compression of 6.7 percent for a constant cross-section cylindrical inlet.

AMS subject classifications: 65Z05, 76K05, 76W05

Key words: Magnetohydrodynamics, hypersonic flows.

1 Introduction

At present, the scramjet appears to be the most promising hypersonic propulsion system due to its simplicity in construction and relatively few components in comparison with other systems [1,2]. The propulsion requirement for high-speed flight varies greatly

*Corresponding author. *Email address:* joseph.shang@wright.edu (J. S. Shang)

 ©2008 Global-Science Press

from take-off to cruising condition and cannot be efficiently supported by a fixed configuration inlet. To improve propulsive efficiency in an operation range, modification of the inlet may be the most cost effective. However once a variable configuration inlet is implemented by an array of compression ramps and boundary-layer control slots, a complicated mechanical flow control must be adopted that leads to a potentially avoidable weight penalty. Meanwhile when operating beyond the design condition, managing and eliminating parasitic effects increases the complicity of the propulsive system. For this reason an alternative, non-intrusive, rapid response, flow control mechanism, other than mechanical means, is very appealing.

Numerous ideas have been advocated for using electromagnetic force for high-speed flow control [3–14]. Some of the research efforts include an externally applied magnetic field in an attempt to accentuate the magneto-fluid-dynamic (MFD) interaction by invoking the Lorentz force in addition to Joule heating [3–9, 12, 13]. Surzhikov and Shang [14] have shown that the Hall current exerts significant influence to the plasma generation via the electron collision process. The Hall current can even suppress the MFD interaction when the value of the Hall parameter attains an exceedingly high value. However, in a relatively weak applied magnetic field, $B \leq 0.2$ Tesla, the interaction is enhanced by the presence of an externally applied magnetic field. In a numerical simulation around a cone in hypersonic flow, Borghi et al. [13] also found that the Hall current can significantly weaken the MFD interaction. All the aforementioned computing simulations are in a general agreement with experimental observations by Bityurin et al. [7] on the effect of Hall current in MFD interactions.

The inefficient plasma generation process has prevented the plasma actuator from becoming a cost effective device for flow control or aerodynamic performance enhancement [15–17]. Shang et al. [9,18,19] conducted a series of side-by-side computational and experimental investigations to show that a small electromagnetic perturbation near the hypersonic leading edge can be amplified by the viscous-inviscid interaction to become an effective flow control mechanism. They first demonstrated that the MFD interaction can perform as a virtual leading edge strake. Using a power supply of 50 Watts to the surface plasma discharge at Mach five, the MFD interaction induces a compression over an immobile surface that acts as though this control surface has executed a one-degree pitching movement [8, 9]. More than a five-degree equivalent pitching angle has been produced by using a total power supply of 350 Watts to the plasma actuator. The similar idea has also been applied successfully to a rectangular constant cross-section area inlet to perform as a virtual inlet cowl [18, 19].

The basic operating principle of the dielectric barrier discharge (DBD) high-speed flow control mechanism is a combination of a small electromagnetic perturbation and a subsequent amplification by the viscous-inviscid interaction. A simple direct current discharge (DCD) near the sharp leading edge of a configuration introduces three mechanisms for flow control; the volumetric Joule heating, convective electrode heating, and the electrostatic force. The dissipative Joule heating is the consequence of electric current movement in a partially ionized gas, the electric conductivity of this medium is typically

lower than one mho/m [19]. The magnitude of the Joule heating associated with the DCD is around 10% of the power required for the surface plasma generation [8,9,14]. For most applications, it has a range up to 10 watts [18, 19]. The electron collision process for plasma generation also results in an electrode temperature around 500 K [8, 9]. In the testing environment of a plasma channel, this electrode temperature is much higher than the model surface temperature and results in a convective heat transfer to the air stream. Based on the tested electrode surface area, the total amount of convective energy transfer is 6.6 watts. Meanwhile an electrostatic force exists adjacent to the electrodes where the space discharge separation occurs in the plasma sheath. The orientation of this force is dictated by the local electric field. The magnitude of the electrostatic force is around 1 kN/m^3, much less than that of dielectric barrier discharge, and is deeply imbedded in the cathode layer [14, 21]. For this reason, all these electromagnetic perturbations exist only in the inner portion of a boundary layer. However, the energy transfer is dominant over that of the momentum transfer for DCD flow control.

To determine the application range of MFD for flow control, the present approach will demonstrate that this flow control mechanism can be equally applicable to a cylindrical inlet. The most obvious choice of the electrode placement is at the sharp leading edge where the flow is laminar and the intensity of the perturbation can be relatively weak, but exerts profound influence on the entire flow field. The classic hypersonic flow theory by Hayes and Probstein describes an inviscid-viscous interaction over a sharp leading edge as the pressure interaction [22]. The induced pressure distribution near the leading edge of a solid surface can substantially alter the growth rate of the displacement thickness of the boundary layer to form a closed feedback loop. The outward deflection of the streamlines and the resulting high-pressure region can reach far downstream. The magnitude of the induced pressure is well-known and can be calculated by a single interaction parameter $\chi = M^3(C/Rey)^{1/2}$. The viscous-inviscid interaction is strongly amplified by hypersonic flows due to its dependence on the cube power of the Mach number. This control mechanism can be repetitiously activated in microseconds. Results from both experimental and computational efforts have shown the chain of events constitute a very effective hypersonic flow control technique [18, 19].

The classic MFD equations at the low Magnetic Reynolds limits are solved to duplicate the experimental observation in a cylindrical inlet model [20]. The partially ionized air models are utilized ranging from a simple phenomenological approximation to the rigorous drift-diffusion theory to describe the nonequilibrium direct current discharge (DCD) [21]. The axisymmetric numerical results are first calibrated with the measured pitot pressure surveys, and then evaluated according to the critical aerodynamic parameters for inlet performance. The temperature and density contours, Pitot and static as well as stagnation pressure distributions are presented to describe the overall flow field structure of the MFD compression.

The paper is organized as follows. In Section 2, the governing equations are introduced. The electrodynamic effects are discussed in Section 3, and the numerical procedure is described in Section 4. The flow-field structure is investigated in Section 5, and

some comparison between the numerical results and the experimental data is given in Section 6. Features of computational simulations are summarized in Section 7. Some concluding remarks are given in the final section.

Nomenclature

$\mathbf{B}$	Magnetic flux density	$\mathbf{E}$	Electrical field strength
e	Electron unit charge	$\mathbf{F}$	Flux vector of the MFD equations
$\mathbf{J}$	Electric current density	M	Mach number
n_e,n_+	Number density of charged particles	p	Pressure
$\mathbf{q}$	Heat flux	Rey	Reynolds number
r	Radius of the polar coordinates	t	Time
$\mathbf{U}$	Dependent variable vector	$\mathbf{u}$	Velocity vector
α	Townsend's ionization coefficient	β	Recombination coefficient
φ	Electric potential	(ξ,η,ζ)	Transformed coordinate
ρ	Density	ε	Electric permittivity
σ	Electric conductivity	μ_m	Magnetic permeability
τ	Shear stress tensor	Γ_e,Γ_+	Flux density of charged particles

2 Governing equations

In most aerodynamic applications of flow control using a plasma actuator, the Magnetic Reynolds number is much less than unity, $\mathrm{Re}_m = u\sigma\mu_m L \ll 1$ [16, 17]. According to the investigated flow condition, the Re_m has a value of 8.48×10^{-6}, thus the governing equations of the low Magnetic Reynolds number approximation are fully justified for the present investigation [16]:

$$\frac{\partial\rho}{\partial t}+\nabla\cdot(\rho\mathbf{u})=0, \tag{2.1}$$

$$\frac{\partial\rho\mathbf{u}}{\partial t}+\nabla\cdot(\rho\mathbf{u}\mathbf{u}-\tau)=\mathbf{J}\times\mathbf{B}, \tag{2.2}$$

$$\frac{\partial\rho e}{\partial t}+\nabla\cdot(\rho e\mathbf{u}-\mathbf{q}-\mathbf{u}\cdot\tau)=\mathbf{E}\cdot\mathbf{J}. \tag{2.3}$$

The electrostatic force term, $\rho_e\cdot\mathbf{E}$, is omitted by the traditional formulation [16, 17]. This simplification in the present analysis is also based on the fact that the electrostatic force is around 43 dyne/cm^3, or 430 N/m^3, which exists within the thin plasma sheath mostly over the cathode and exerts downward. It is negligible in comparison with the inertia of the oncoming hypersonic flow. Again in the absence of an applied external magnetic field to the DCD, the Lorentz force, $\mathbf{J}\times\mathbf{B}$ in equation (2.2) is also relatively insignificant, but is retained for a possible externally applied magnetic field.

The governing partial differential equation system is identical to the Navier-Stokes equations except the non-zero source terms. The DCD has the maximum charged particle number density over the cathode and has a maximum value around 8.8×10^{11}/cc, the electrical conductivity is less than 1 mho per meter locally. At the experimental stagnation

pressure of 580 Torr (7.47 Kpa) and Mach number of 5.15, the air number density in the test section is 1.57×10^{17}/cc; thus the mass fraction of the charged particles is $10^{-5}$to 10^{-6}. It is therefore justifiable to consider only the transport properties of the weakly ionized air and to neglect the effects of the nonequilibrium chemical kinetics.

For the MFD compression, the electromagnetic perturbation enters the interaction mostly as the volumetric Joule heating and convective electrode heating. These two fundamentally heat transfer processes occur at vastly different time scales; the former takes place at the instant when the plasma is ignited on the order of microseconds, and the heat release is confined to within a few Debye lengths immediately above the electrodes. The convective heat transfer on the other hand will not reach an equilibrium state until a few minutes later [8, 9]. The heating effects thicken the displacement thickness of the shear layer on the inlet surface, however it is additive. To model this perturbation, a wide range of formulations of the electromagnetic perturbation is possible, but the total amount of energy released to the air stream is calculated from the direct current gas discharge based on the drift-diffusion theory. Surzhikov and Shang [21] have successfully developed a model of a three-component plasma (neutral, electron, and ion) and two-temperature plasma:

$$\frac{\partial n_e}{\partial t}+\nabla\cdot\Gamma_e=\alpha(E,p)\,|\,\Gamma_e\,|-\beta n_+ n_e, \tag{2.4}$$

$$\frac{\partial n_+}{\partial t}+\nabla\cdot\Gamma_+=\alpha(\mathbf{E},p)\,|\,\Gamma_e\,|-\beta n_+ n_{e,}, \tag{2.5}$$

$$\Gamma_e=n_e\mathbf{u}-D_e\nabla n_e-n_e\mu_e\mathbf{E}, \tag{2.6}$$

$$\Gamma_+=n_+\mathbf{u}-D_+\nabla n_++n_+\mu_+\mathbf{E}. \tag{2.7}$$

In the above formulation, α (E, p) and β are the first Townsend ionization coefficient and recombination coefficient. The parameters μ_e and μ_+ are the electron and ion mobility, and D_e and D_+ are the electron and ion diffusion coefficients [15, 21]. The electrical current density appears in the low Magnetic Reynolds number approximation as:

$$\mathbf{J}=e(\Gamma_+-\Gamma_e). \tag{2.8}$$

A compatible electrical field intensity, **E**, of the discharge domain is obtained by satisfying the charge conservation equation [14, 18]. This equation is further simplified in a globally neutral plasma by introducing an electrical potential function,

$$\mathbf{E}=-\nabla\phi.$$

The electrical field intensity is then the solution of the well-known Poisson equation of plasmadynamics associated with the net space charge density, ρ_e.

$$\nabla^2\phi=-\rho_e/\varepsilon. \tag{2.9}$$

For the Poisson equation, the adopted boundary conditions are straight forward; the electric potential across the electrodes is imposed on anode over the grounded cathode.

The vanishing normal gradient condition is applied on the dielectric surface and all far-field boundaries.

The initial values and boundary conditions, as well as, the numerical procedure are directly usable from the cumulative knowledge from the CFD discipline [8–12]. For the velocity components, the free-stream and the no-change condition are prescribed at the entrance, far field, and exit boundaries of the computational domain respectively. The no-slip condition applies to all the velocity components on the inlet solid surface. The constant wall temperatures are imposed on the inlet surface (270 K), as well as on the surface of electrodes to duplicate the experimental condition [18, 19]. Finally, the surface pressure is evaluated by the vanishing normal pressure gradient condition locally.

The initial values and boundary conditions of the plasma model for a numerically stable procedure have been found through a series of sustained research efforts [8–10, 14, 21]. A key element in determining the boundary conditions is specifying the electron number density on the cathode for the secondary emission phenomenon. This physical requirement is met by specifying that the normal component of the electron flux at the cathode be proportional to its ion counterpart [21]:

$$\Gamma_e \cdot n = -\gamma \Gamma_+ \cdot n. \tag{2.10}$$

All numerical results are obtained by solving the time-dependent conservation laws in mass-averaged variables. The spatial discretization involves a semi-discrete finite-volume scheme [23, 24]. The upwind-biasing approximation is applied to the convective and pressure terms and central differencing is used for the shear stress and heat transfer terms.

3 Electrodynamic effects

The non-equilibrium chemical kinetics associated with direct current discharge (DCD) or dielectric barrier discharge (DBD) is well known and has been thoroughly studied by treating 143 reactions among 30 reacting species [25]. The complex chemical composition of the weakly ionized gas is fully recognized but the most profound effect for fluid dynamic application is the transport property of the electric conductivity. In spite of the long history of DCD and DBD development, the critically important electromagnetic field parameter for magneto-fluid-dynamic interactions is still largely uncertain. In particular, there is a very limited amount of basic knowledge on the interaction of the charged and neutral particles in an electromagnetic field, which in turns raises a series of questions on whether the charge separation over the electrode or the plasma heating has played a dominant role for the observed discharging gas phenomenon [9, 10].

In surface plasma generation based on electron collision process, the Townsend's mechanism controls the multiple primary avalanches and secondary emission and ultimately maintains the discharge [15]. The charged particle number density is generally

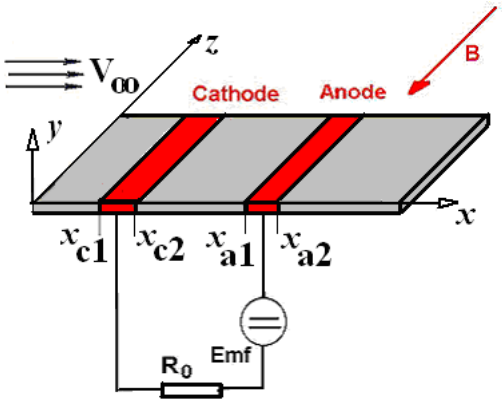

Figure 1: Side-by-side electrode placement of DCD for flow control.

limited to the order of magnitude of 10^{12} per cubic centimeter. The generated plasma consists of electrons in a highly excited state but the heavy ions retain the thermodynamic condition of its surrounding environment. Therefore the weakly ionized gas is normally far from thermodynamic equilibrium. Nevertheless the force diffusion, including the ambipolar diffusion, profoundly modifies the transport properties of the ionized medium. The description of the weakly ionized gas has become the most challenging issue for both experimental and computational investigations [4–12].

Two fundamental mechanisms of charged particle dynamics are the drift velocity and the ordinary diffusion [15–17]. This behavior is independent of how the gas discharge is generated and is the fundamental mechanism in the drift-diffusion plasma model [21]. The DCD is dictated by the externally applied electric field; therefore the structure of the DCD has a strong dependence to the electrode configurations. The configuration widely adopted by flow control is the side-by-side electrodes arrangement in which the cathode is placed upstream to the anode and embedded in the control surface. A typical configuration is presented in Fig. 1. Both electrodes are embedded on the control surface and are separated by a short distance. The surface plasma is activated by applying an electromotive force across and the current for plasma generation is regulated by the resistance of the external circuit. In this electrode placement, the electric field orientation is not as well-defined as in the classic parallel configuration and has led to some speculations regarding the modeling issues [3–9]. For this reason, simplified computing simulations on a reduced spatial dimension and in a quiescent air are included in here to illustrate the basic discharge physics.

The governing equations including the Poisson equation for space charge, equations (2.4) through (2.7), in an iterative solving scheme can be expressed in flux vector form as

$$\frac{\partial \mathbf{U}}{\partial t} + \nabla \cdot \mathbf{F} = \mathbf{R}, \tag{3.1}$$

where the dependent variable is $\mathbf{U} = \mathbf{U}(\phi, n_e, n_+)$, the flux vector is given as

$$\mathbf{F} = \mathbf{F}(\nabla\phi, \Gamma_e, \Gamma_+),$$

and the inhomogeneous right-hand-side terms become

$$\mathbf{R} = \mathbf{R}[-\rho_e/\varepsilon, \alpha(E,p)|\Gamma_e| - \beta n_+ n_e, \alpha(E,p)|\Gamma_e| - \beta n_+ n_e].$$

The charge number density is defined as $\rho_e = e(n_+ - n_e)$ which vanishes away from the electrode regions to maintain the plasma global neutrality.

In the present analysis, the system of governing equations is solved by a cascading alternating direction implicit (ADI) scheme in delta form. In this formulation, the temporal advancement of the solution is directly driven by the law of physics. For a two-dimensional approximation, the discretized governing equations appeared as;

$$\frac{\delta(\Delta u)^*}{\delta t} + \left(\frac{\delta \mathbf{F}}{\delta x_i}\right)^* = \mathbf{R}, \tag{3.2}$$

$$\frac{\delta(\Delta u)^{n+1}}{\delta t} + \left(\frac{\delta \mathbf{F}}{\delta x_j}\right)^{n+1} = \left(\frac{\Delta u}{\Delta t}\right)^*. \tag{3.3}$$

Because the dominant electrodynamic force of the DCD for flow control is manifested by the electrostatic force and Joule heating, the computed electric field and current for the side-by-side electrode configuration are included for better understanding. All numerical results were obtained from a grid system consisting of 19,200 grid points (160×120). The grid-point clustering is implemented normal to the electrode surface as well as the electrode edges. The finest grid-point spacing is in the order of magnitude of a thousandth of the electrode length.

The side-by-side DC discharge is generated by an EMF of 2000 V and at an ambient pressure of 5 Torr. In the simulation, the cathode and the anode have the same length of 0.5 cm each and are separated by a dielectric spacer of 1 cm in length. The cathode is placed on the left of the anode with edges being located at 1.0 and 1.5 cm in the computational domain. The electrical potential across the electrodes reduces to 430 V and the electric field intensity attains a value of 10^8V/cm, and the total current in the discharging field yields a value of 5.23 mA. In Fig. 2, the electric field intensity line is superimposed over the ion number density contour. The high concentration of ion number density at the edge of electrodes with the shortest separation distance is clearly and correctly displayed and the maximum ion number density has a value of 5.76×10^{10}/cc over the edge of the cathode. Most importantly, the strong electrical field is perpendicular to the cathode. In application for flow control, the resultant electrostatic force is exerted downward toward the cathode which can not be supported by the shear stress to alter the flow structure but transmits directly to the cathode.

Similarly, the electron number density distribution and the superimposed discharging current are depicted in Fig. 3. The electrons are concentrated mostly over the anode at

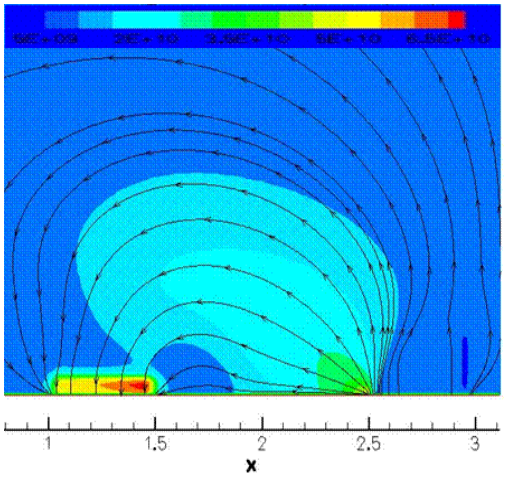

Figure 2: Ion number density contour and electric field intensity vector line, EMF=2000 V, p=5.0 Torr.

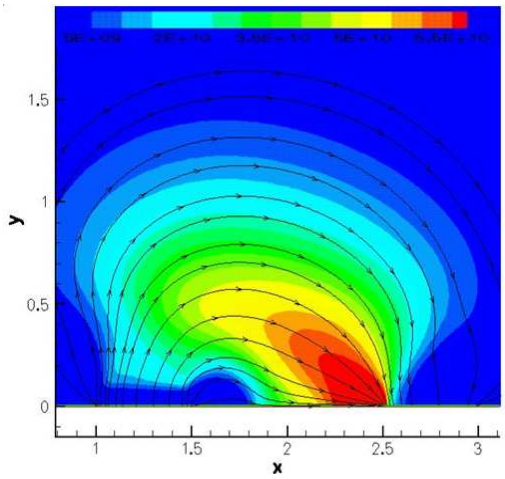

Figure 3: Electron number density contour and electric current density line, EMF=2000 V, p=5.0 Torr.

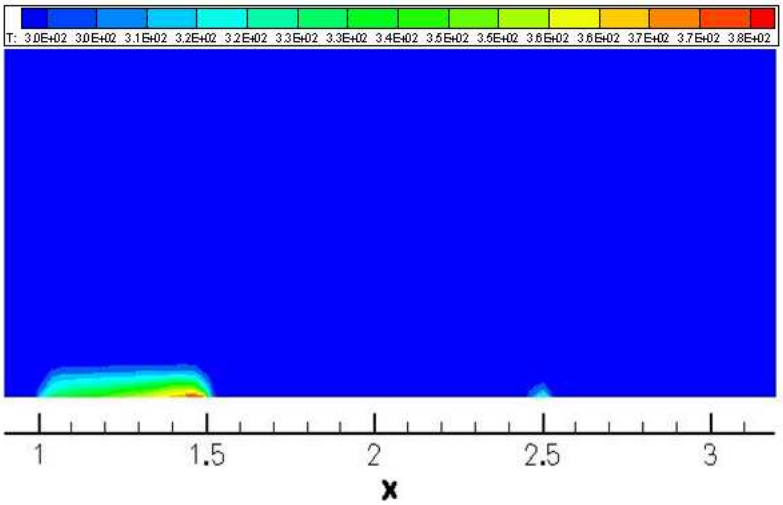

Figure 4: Joule heating contour over the side-by-side electrode configuration, $\phi_{cathode}=210V$, $I=5.23mA$

the nearest edge toward the cathode. The maximum electron number density of the discharging field is 3.02×10^{10}/cc. The electrons are nearly absent in the cathode layer except the secondary emission from the electrode which is easily observed. The averaged thickness of the cathode layer from the computed simulation is 0.125 cm and is comparable to the classic one-dimensional result of 0.15 cm by Von Engel and Steenbeck [26].

In Fig. 4, the Joule heat distribution over the side-by-side electrode arrangement is given. The volumetric heating occurs mainly within the cathode layer and with a significant concentration over the edge of the cathode that is located closest to the anode ($x=1.5$ cm). A hot spot also located immediately over the anode at $x=2.5$ cm but with a

much less heat intensity. The numerical result has duplicated the physical phenomenon in which the dissipative heating is pronounced over the edges of the electrodes. For the present simulation, the Joule heating released to the entire discharging field is 1.30 J/s. This value is relatively small in comparison with the total amount of power for the surface DC plasma generation, 21.52 J/s.

However, the thermal energy is released directly into the interior domain instead of onto the boundary of the control volume. In flow control application over a solid surface, this form of energy deposition is not achievable by purely aerodynamic means and is extremely effective to alter the flow field structure. The additional energy source creates a local expansion to thicken the displacement thickness of the attach shear layer as a triggering mechanism for a chain of events of viscous-inviscid and magneto-fluid-dynamic interactions. Since the energy released by DC discharge appears as a small perturbation it must be amplified by viscous-inviscid interaction to become a viable flow control mechanism [14, 15].

4 Numerical procedure

For study the magneto-fluid-dynamic interaction phenomenon the governing equations, equations (2.1) through (2.7) are solved closely coupled. The flux-difference splitting procedure for shock capturing, the flux vectors at the control surface are written as the solution to the approximate Riemann problem:

$$\begin{aligned}\delta\mathbf{U}_i=&\frac{1}{2}[\mathbf{F}(\mathbf{U}_L)+\mathbf{F}(\mathbf{U}_R)-|M_{inv}|(\mathbf{U}_R-\mathbf{U}_L)]_{i+\frac{1}{2}}\\&-\frac{1}{2}[\mathbf{F}(\mathbf{U}_L)+\mathbf{F}(\mathbf{U}_R)-|M_{inv}|(\mathbf{U}_R-\mathbf{U}_L)]_{i-\frac{1}{2}},\end{aligned}\tag{4.1}$$

where $\mathbf{U}_L$ and $\mathbf{U}_R$ are interpolated values of the dependent variables, ρ , ρu, ρv, and ρe at the interface of the control volume and Minv is the Jacobian matrix of the inviscid or convective terms [23].

A slope limiter is also used to control the discontinuous pressure jumps at the shock front. Time advancement is implicit to solve that the flows have a steady state asymptote. A min-mod limiter is adopted for the present computations:

$$(\mathbf{U}_L)_{i+\frac{1}{2}}=\mathbf{U}_i+\frac{1}{4}[(1-\kappa)\nabla+(1+\kappa)\Delta]_i,\tag{4.2}$$

$$(\mathbf{U}_R)_{i+\frac{1}{2}}=\mathbf{U}_{i+1}-\frac{1}{4}[(1-\kappa)\Delta+(1+\kappa)\nabla]_{i+1},\tag{4.3}$$

where the one-side difference operators are; $\Delta = \mathbf{U}_{i+1} - \mathbf{U}_i$ and $\nabla = \mathbf{U}_i - \mathbf{U}_{i-1}$. The value of κ is assigned a value of -1 to yield the second-order fully-upwind differencing approximation.

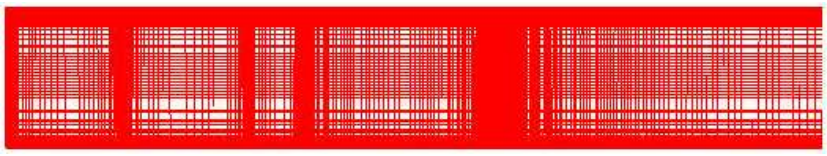

Figure 5: 93×301 mesh system.

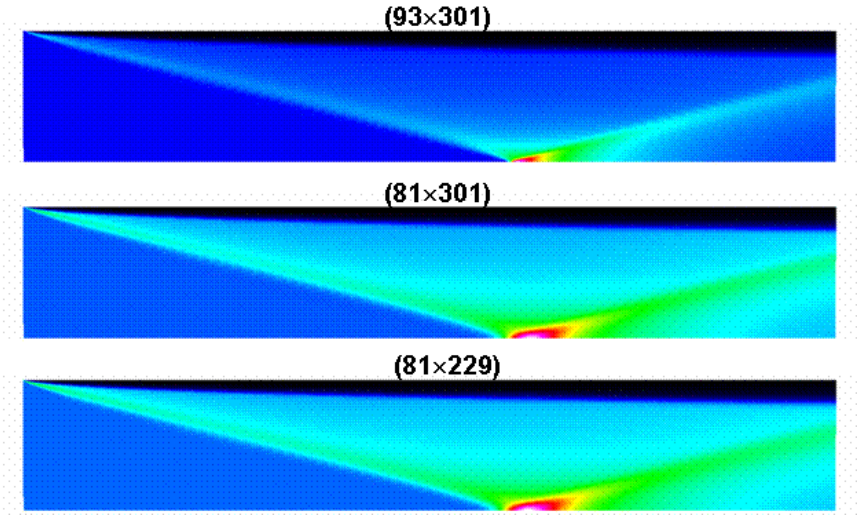

Figure 6: Comparison of density contours on three different grid systems, $M_\infty = 5.15$, $Rey = 2.52\times10^5$, $p_\infty = 0.9Torr$.

The min-mod operators are defined as;

$$\nabla = minmod[\nabla, \frac{3-\kappa}{1-\kappa}\Delta], \tag{4.4}$$

$$\Delta = minmod[\Delta, \frac{3-\kappa}{1-\kappa}\nabla]. \tag{4.5}$$

For convergence acceleration, a three-level mesh sequencing of the multigrid technique is applied [24].

For the axisymmetric configuration, only the upper half of the radial plane is included in the computational domain [20]. The numerical simulations are generated on three mesh systems, (81×229), (81×301) and (93×301) to better capture the invert conical shock originating from the leading edge of the model. The minimum grid spacing immediately adjacent to the sidewall is one hundredth of the laminar boundary thickness at the exit plane (4.37×10^{-4}cm). A compressed mesh is also implemented at the leading edge of the inlet with four streamwise cross-section planes to define the freestream. A high mesh density is also provided at the edges of electrodes and the anticipated apex of the conical shock for better numerical resolution. The finest mesh system of the present investigation is depicted in Fig. 5.

In Fig. 6, the computed density contours in the upper-half-plane of the flow field on three progressively refined mesh systems are presented. The coarsest mesh has only the high grid density in the inner domain of the boundary layer, leading edges of the model, and the edges of electrodes (81×229). The medium mesh system is enriched by an additional mesh clustering at the anticipated conical shock apex (81×301). The finest mesh system includes a further mesh space refinement at the axis of symmetry (93×301). For all mesh system used, the ratio between the finest axial and radial mesh spaces is a factor of ten ($\Delta x = 4.37\times10^{-3}$cm, $\Delta r = 4.37\times10^{-4}$cm). The finest mesh spacing is located immediately adjacent and normal to the inlet sidewall. As clearly shown in Fig. 6; all numerical simulations capture the essential feature of the bi-conical shock structure. The locations of the shock apex are better defined as the mesh density is enriched. The result from the refined mesh shows a progressive movement of the shock apex toward upstream, however the maximum deviation among all results is 0.8%.

5 Flow-field structure

The present numerical simulation duplicates the experimental effort to generate a virtual variable geometric inlet cowl by using the DCD within a constant cross-section cylindrical inlet model [20]. The freestream Mach number has a nominal value of 5.15 and the stagnation temperature is 270 K; thus the static temperature of the unperturbed freestream is 43 K. To ensure a stable inflow condition for the channel with the cylindrical inlet model, tests are conducted at two stagnation pressures, 370 and 580 Torr. These conditions produce two Reynolds numbers based on model lengths of 1.66×10^5 and 2.52×10^5 respectively [20]. In the data reduction process, the most reliable data were found at the higher stagnation pressure condition; therefore the presented numerical simulation concentrates on this experimental condition.

For the constant cross-sectional area inlet model, the overall length of the model is 10.16 cm and outer and inner diameters are 4.44 cm and 3.49 cm respectively. The cathode and anode are embedded in the sidewall normal to the x coordinate. The cathode ring has a width of 1.43 cm and the width of the anode is 0.64 cm. The separation distance between the electrodes is 1.59 cm and the weakly ionized air is sustained by an electric potential of 480 V for currents from 50 to 150 mA. The cathode is placed at the leading edge of the model which has an outward bevel of 20 degrees; the nominally sharp leading edge actually has a small radius of curvature of 0.127 mm. The actuated DCD in the cylindrical inlet is depicted in Fig. 7. The DC discharge is viewed from the exit of the duct and at an oblique angle from the axis. The dominant visual feature of the discharge is the glow over the electrodes and the refection from the glass sidewall. Under this testing condition, the discharge current density on the anode is 6.78 mA/cm^2.

It is interesting to note that a trivially simple cylindrical inlet generates a rather intriguing shock wave structure within the hypersonic inlet. The viscous-inviscid interaction at the leading edge induces an inverted conical shock and the apex of the shock is

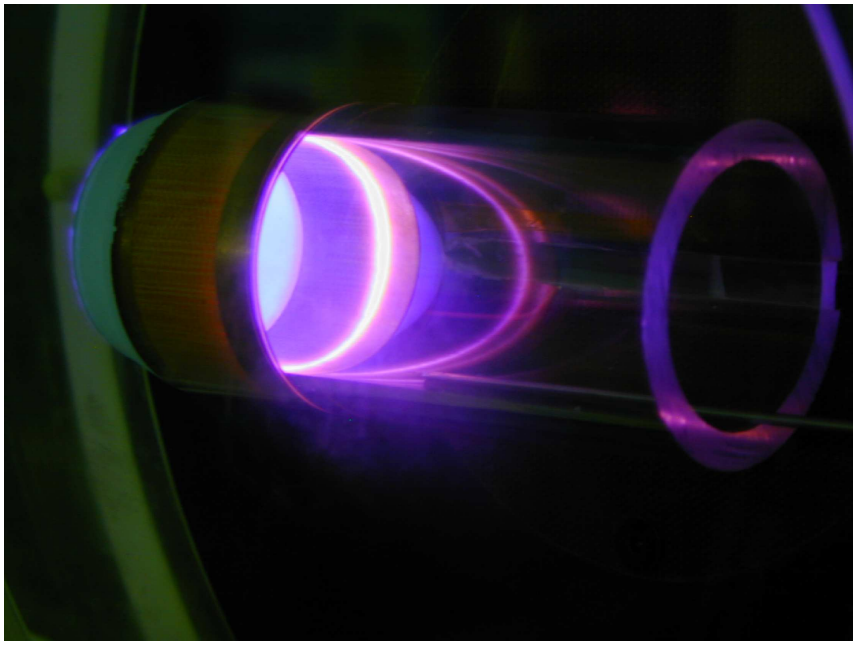

Figure 7: Activated DCD, ϕ=480 V, I=50mA, $M_\infty = 5.15$, $Rey = 2.52\times10^5$, p_∞=0.9 Torr.

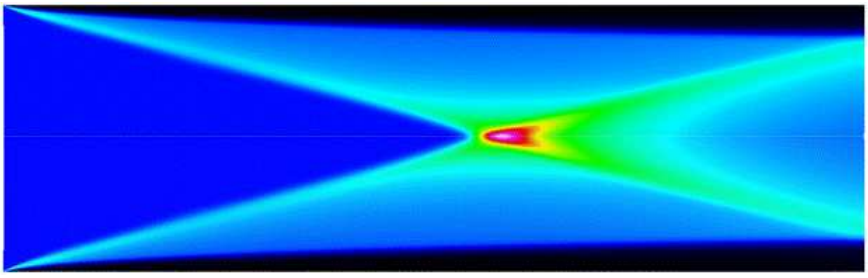

Figure 8: Density contour within the cylindrical inlet, $M_\infty = 5.15$, $Rey = 2.52\times10^5$, p_∞=0.9 Torr.

located on the axis of symmetry. Downstream of the apex, the reflected shock wave continuously propagates towards the exit plane. In Fig. 8, the computed density contours within the inlet are given; the numerical result is generated on the coarsest mesh system but still describes the basic shock wave structure. At the apex of the conical shock, the basic wave structure is uncertain. Since the stream is converging toward a single point and diverging immediately afterward, a Mach reflection is possible [27, 28]. The Pitot pressure probe survey at the apex reveals a sharp spike, indicating a drastic shock structure adjustment at the shock focus. Unfortunately, this phenomenon occurs on the axis of symmetry where the numerical result must be generated on a line of a removable singularity. Instead of utilizing multiple numerical algorithms or a general 3D formulation, a mesh refinement approach is adopted in the present study.

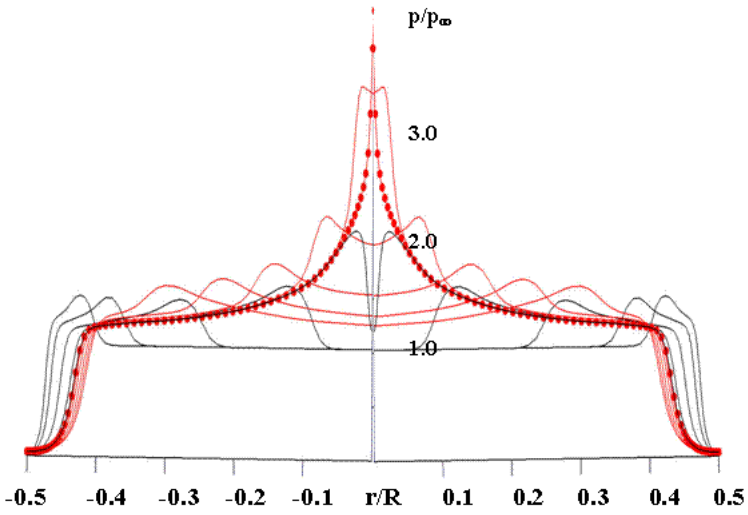

Figure 9: Static pressure Profiles within the cylindrical Inlet, $M_\infty = 5.15$, $Rey = 2.52\times10^5$, p_∞=0.9 Torr.

Pressure profiles at different streamwise locations generated from the finest mesh systems are given in Fig. 9. In order to better describe the static pressure patterns, the profiles upstream of the shock apex are designated in black and the downstream variations are presented as the red traces. At the shock apex the pressure profile is presented in red connected discrete points. The numerical simulations capture a spike pressure behavior at the conical shock apex. Upstream of this point, the pressure profiles reveal a converging conical shock toward the apex. Immediately upstream of this location, the pressure distribution at the axis of symmetry exhibits a dip. Since there is no physical observation that can support this behavior, it is believe to be a numerical artifact. Downstream of the shock apex, the numerical results indicate a divergent conical shock structure and increasing thickness of the wall shear layer. These computed results seem to indicate that the streamwise numerical resolution is sufficient to determine the location of the apex of the conical shock.

6 Comparison with experimental data

The direct current discharge is introduced into the internal flow field of a constant cross-sectional area cylindrical model as a small perturbation. The interaction between the electromagnetic effect and the fluid dynamics is linked through the outward flow deflection by the thickened displacement thickness. In supersonic and hypersonic flow, the rate of change by the displacement thickness becomes the key parameter for the induced oblique shock in the viscous-inviscid interaction. The rate of change in displacement thickness directly corresponds to the power input for plasma generation. This observation can be made in Figs. 10 and 11.

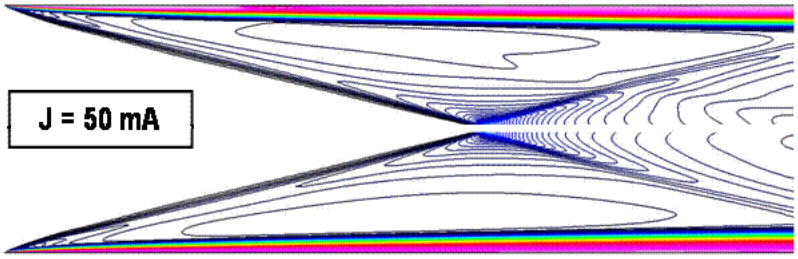

Figure 10: Simulated temperature field with/without DCD, $\phi=402V$, $I=50mA$, $Rey=1.66\times10^5$.

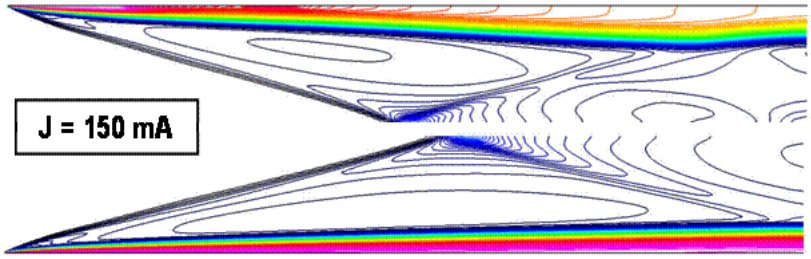

Figure 11: Simulated temperature field with/without DCD, $\phi=460V$, $I=150mA$, $Rey=1.66\times10^5$.

In Fig. 10, the composite temperature distributions for the inlet with and without an activated DCD at an electric potential of 402 volts and circuit current of 50 mA are given. The simulated computation duplicates the experimental condition including the elevated electrode surface temperatures. According to the best estimate, the surface temperature of the cathode is 500 K and the anode has a lower value of 350 K [9, 19]. In this graph, the activated DCD result is depicted in the upper half plane and the deactivated flow in the lower half plane. As it was anticipated, at the low plasma generation power the Joule heating is determined to be less than 2 watts and the induced magneto-fluid dynamic compression is relatively small. This observation can be easily made in this comparative presentation; the resultant oblique shock is slightly steepened and intercepts the axis of symmetry upstream of the unperturbed flow.

However, the result is drastically different for the higher plasma power input in Fig. 11. The comparative study is generated by the actuator powered by 69.0 watts; the applied electric field potential of 460 volts and the circuit current of 150 mA. An induced oblique shock now possesses a significant strength so that the oblique shock continuing after the shock focus impinges on the inner surface of the inlet model. The impinging shock generates an unexpected and additional viscous-inviscid interaction near the exit plane of the inlet at the lower Reynolds number condition, Rey=1.66×10^5. In the numerical simulation, the adverse pressure gradient even triggers incipient flow separation near the exit plane at the relatively low Reynolds number flow condition. Unfortunately, this result is not directly verifiable from the experimental observations [19].

This specific phenomenon can be further verified by the comparison of the streamwise Pitot pressure distributions along the axis of the inlet model in Fig. 12. The computed and measured results of the activated DCD are designated by the solid line and filled square symbols for the plasma activated case and by the dash line and filled circles for the deactivated condition. The computing simulations do not include the slightly blunt leading edge, thus have a weaker oblique shock. As a consequence, the shock focus is consistently formed downstream of the experimental observation and the divergent conical shock after passing through the shock focus does not impinge on the inlet side wall. The impinging shock of the experiments creates an adverse pressure gradient near the inlet exit plane which can induce either flow instability or incipient flow separation for the low Reynolds number flow. This behavior is different from the numerical simulations of the sharp leading edge cylindrical inlet in which the divergent shock exits the inlet uninterrupted.

For the axisymmetric configuration, the characteristic thicknesses of the boundary layer are thinner in comparison with a two-dimensional counterpart. According to Mangler [29], the thickness is reduced by a factor of $\sqrt{3}$ on a conical configuration at the identical Reynolds number. The induced pressure is thus accordingly smaller and more difficult to resolve than the rectangular inlet [18, 19]. An added complication for the experimental effort is that the blockage of the inlet model for the blow-down free jet facility has approached its limit. A small fluctuating back pressure from the vacuum pumps amplifies the model blockage in the free jet. The back pressure was carefully monitored during testing to maintain values of 8 ± 0.5 mm HG, but a constant value was not sustainable. For this reason and the shock impingement interactions, the test data exhibit a wider data scatter near the exit which indicates the possibility of a local separated flow region and reflecting by the unsteady flow pattern [24]. In spite of the local discrepancy, both measured and computed results indicate a perceptible magneto-fluid-dynamic compression effect.

The comparison of Pitot pressure data and computing simulations in the axial direction, but at an off-axis location, $r/R = 0.3$, is depicted in Fig. 13. Although the data indicate stronger shock strength than the computing simulation downstream of the conical shock focus, reasonably good agreement between experimental and computational results has been reached. In addition, these results further confirm the fact that the large data scattering band near the inlet exit is confined to a region close the wall of the inlet. More importantly, the data and computational results both clearly show a measurable magneto-fluid-dynamic compression produced by the simple DCD at the entrance region of the cylindrical inlet.

Additional verifications of the numerical simulations is performed by comparing to experimental observations at a few cross-sectional planes of the inlet are also included. The Pitot pressure profiles at the axial location of $x/D = 1.33$, upstream of the conical shock focus, is presented in Fig. 14. It becomes obvious that the data is not symmetrical because of the misalignment of the model with respect to the centerline of the plasma channel. This pattern has also been detected from the experimental measurement of the

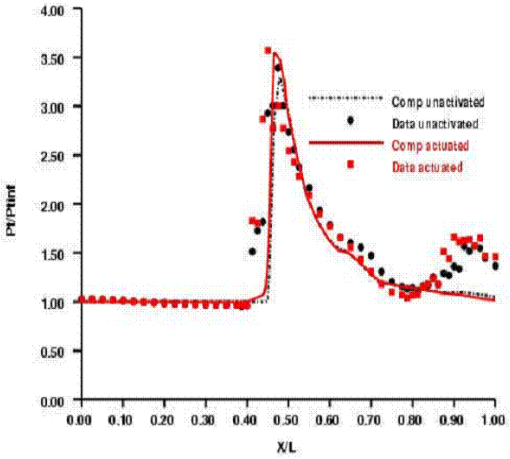

Figure 12: Comparison of Pitot Pressure distributions along the axis of symmetry, $M_\infty = 5.15$, $Rey = 2.52\times10^5$, $p_\infty = 0.9Torr$.

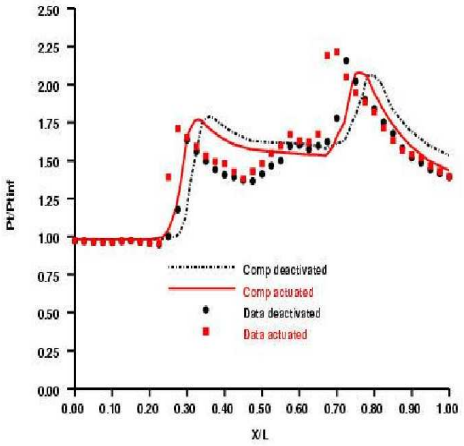

Figure 13: Comparison of off axial Pitot pressure distributions with/without DCD, $M_\infty = 5.15$, $Rey = 2.52\times10^5$, $p_\infty = 0.9Torr$.

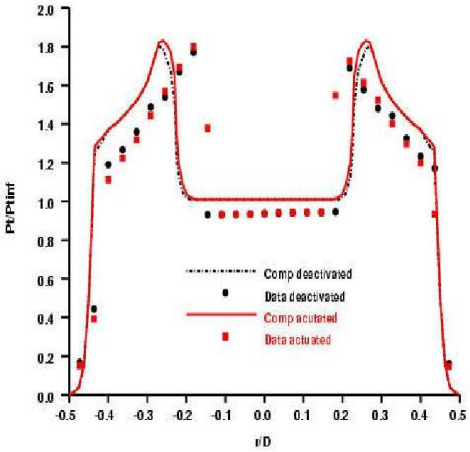

Figure 14: Pitot pressure profiles upstream of the conical shock focus, $x/D = 1.3$, $M_\infty = 5.15$, $Rey = 2.52\times10^5$, $p_\infty = 0.9Torr$.

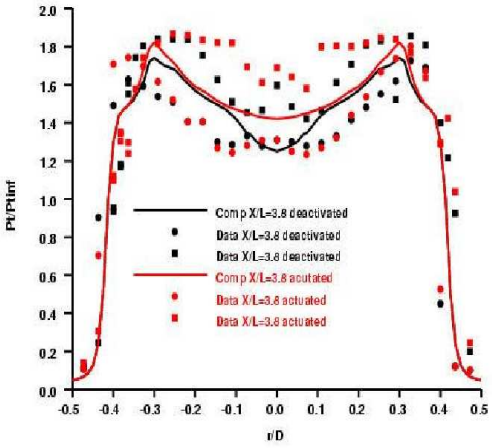

Figure 15: Pitot pressure profiles near inlet exit plane, $x/D = 3.8$, $M_\infty = 5.15$, $Rey = 2.52\times10^5$, $p_\infty = 0.9Torr$.

horizontal and vertical Pitot pressure surveys [20]. In spite of this fact the computing simulations reproduce all the key features of the leading edge and DCD induced oblique shock. The agreement has been reached in the prediction of the shear layer thickness and the existence of an inviscid core. The overpredicted core size is completely consistent to the fact that the induced oblique shock from a slightly blunt leading edge possesses a greater shock angle and smaller inviscid core. At this upstream stream location, the difference between the deactivated and activated DCD flow fields is relatively small and is within the data scatter but is highlighted by the computed results.

Unfortunately, the important comparison of Pitot pressure profiles near the inlet

exit plane cannot lead to a definitive quantification. The basic issue is a possible time-dependent or unrepeatable flow behavior at the inlet exit plane. In Fig. 15, two sets of data taken at different dates are presented together with computing results at a streamwise location of $x/D=3.8$. The computational simulations with and without DCD actuation are embedded within the data bands. However an important observation is beyond doubt in that the magneto-fluid-dynamic compression has been generated by the surface plasma. From the integrated Pitot pressure data across the exit plane, the increased value produced by the DCD has a range from 8.4% to 12.6%. The computational simulations yield a value of 6.7% at the plasma power of 69.0 watts.

This computed value is lower than the MFD compression gain in Pitot pressure within a constant cross-sectional area rectangular inlet of 11.7% [19]. The two different inlet models are designed for the same cross sectional areas of 9.58 cm^2 and the DCD is supplied by similar power (69.0 versus 64.0) for the rectangular inlet. This difference may be partially attributable to the Mangler effect of boundary-layer scaling or more precisely the reduced displacement thickness over an axisymmetrical configuration [29]. The direct comparison of computed static pressure profiles at the exit plane of the rectangular and cylindrical inlet is presented in Fig. 16. Although the shock structures are different from the two inlet configurations, the results of the MFD compression are clearly displayed at the identical inlet entrance flow conditions. The additional compression gain over the unperturbed flows is generated by the electromagnetic perturbation to the shear layer at the leading edge of the inlet and is amplified by the viscous-inviscid interaction. The magnitude of the MFD compression within the rectangular inlet is slightly greater than that of the cylindrical configuration. According to the pressure interaction theory, the compression gain will increase at a higher Mach number [22].

7 Features of computational simulations

The basic component of the MFD compression is the magnitude of the electromagnetic perturbation that initiates the viscous interaction. For a DCD it is the intensity of the externally applied electric field through the surface discharge. The electromagnetic perturbation introduces a thermal perturbation to increase the growth rate of the displacement thickness of the boundary layer. The subsequent inviscid-viscous interaction generates a coalescing oblique shock wave for the MFD compression. Since the mechanism is a small perturbation, the compression is generated by a minimum amount of entropy increment. This fact can be verified easily by comparison of the stagnation pressure profiles at the inlet exit. In Fig. 17, the stagnation pressure distributions at this location with and without the activated DCD, under identical conditions of the experiments, are depicted together. The DCD is produced with 460 volts and 150 mA [20]. Under this discharging condition the difference in stagnation pressure profiles is negligible which means the additional and small gain in MFD compression occurs without a detrimental effect.

The following two graphs, Figs. 18 and 19, summarize the application range of a

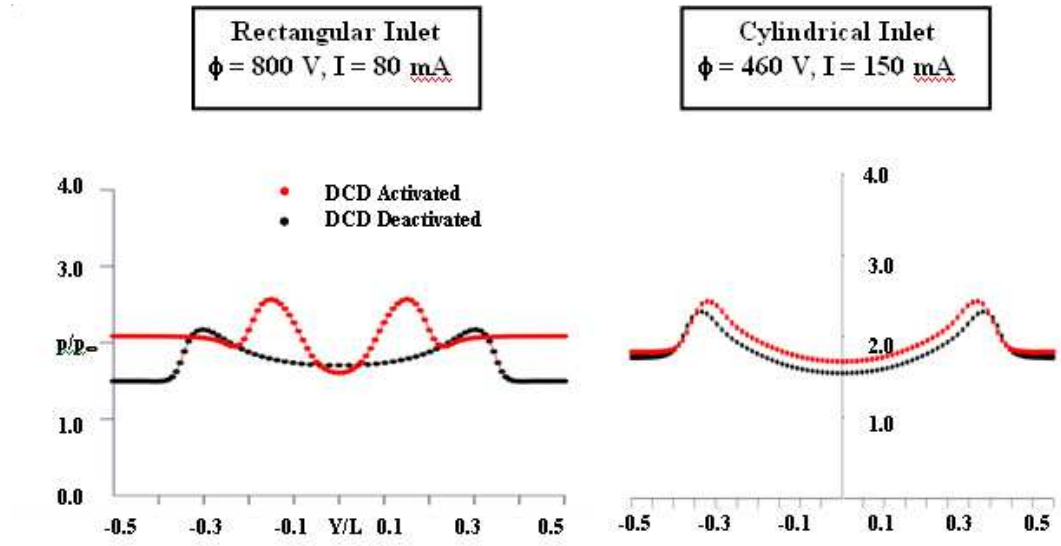

Figure 16: Comparison of computed static pressure profiles at exit of rectangular and cylindrical inlet.

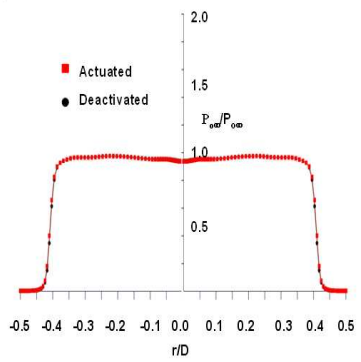

Figure 17: Comparison of stagnation pressure profiles with/without DCD at exit, $M_\infty = 5.15, Rey = 2.52\times10^5, p_\infty = 0.9 Torr, \phi = 430V$.

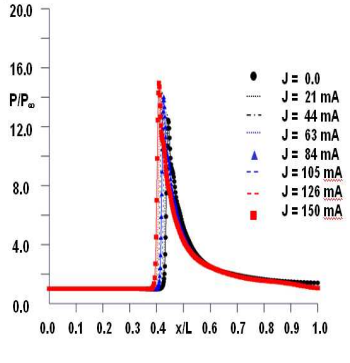

Figure 18: Compression generated by a range of current in external circuit, $M_\infty = 5.15, Rey = 2.52\times10^5, p_\infty = 0.9 Torr, \phi = 430V$.

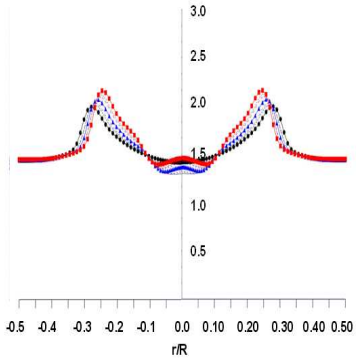

Figure 19: The static pressure profiles at exit for a range of discharge currents, $M_\infty = 5.15, Rey = 2.52\times10^5, p_\infty = 0.9 Torr, \phi = 430V$.

DCD for flow control. In order to examine a large group of DCD conditions, the thermal perturbation is imposed by a simple phenomenological model by matching the Joule heating with a heat source. In practical application, the electric potential is maintained at a constant value and the current flow is modulated by the electrical resistance in the external circuit.

In Fig. 18, eight static pressure distributions along the axis of the cylindrical inlet are presented for external circuit current from 0.0 to 150 mA. The maximum discharge current is determined from the experimental observation beyond which a diffusive discharge becomes constricted. The resultant oblique shock by MFD compression increases its strength and the shock angle becomes steeper to intercept the axis of symmetry of

the cylindrical inlet at an upstream location. A rapid expansion ensues downstream and the greater the compression the more rapid the expansion occurs. Therefore, an optimal placement of the cathode can generate a desired compression at a specific location of the inlet.

The corresponding static pressure profiles at the inlet exit plane are given in Fig. 19. The change in the profile for different discharge currents is rather limited, thus only the current of 0.0, 84, and 150 mA are highlighted. The main feature of the increased compression is concentrated near the shock front and the downstream expansion is proportional to this strength. In fact, the expanded pressure level at the axis of the inlet by the higher discharge current is actually below the unperturbed condition. This expansion within the inlet can be adjusted by the placement of the electrode closer to the inlet exit to yield a higher compression gain at the inlet exit. However, the induced pressure plateau by the pressure interaction will be lower because the interaction parameter χ, is inversely proportional to the Reynolds number based on the running length from the leading edge. This observation suggests an optimal electrode placement has not been used in the studied configuration.

8 Concluding remarks

The concept of using an electromagnetic perturbation to enhance the pressure interaction for MFD inlet compression has been further demonstrated. The range of application for the high-speed plasma actuator has been extended to include a cylindrical inlet. The power input for plasma generation in the present investigation is limited to 69.0 watts (φ = 460 V and I=150 mA); therefore the effect of magneto-aerodynamic compression is small. The induced magneto-fluid-dynamic compression is determined to be 6.7% over that of the unactivated inlet flow. A reasonable agreement is achieved between experimental and computed results, but a crucial quantification by comparing the measured Pitot pressure profiles near the constant cross-sectional area cylindrical inlet is not achieved, because of the rather large data scattering. An effort shall be sustained to better understand the underlying physics.

The effectiveness of the MFD compression is expected to be less than that of a rectangular inlet partially due to the Mangler effect, but the induced MFD compression is still perceptible and detected by both the experimental and computational investigations. The compression ratio is rather modest at a low power supply and the relatively low free-stream Mach number. Under this circumstance, the MFD compression gain is achieved without any loss of the stagnation pressure by the virtual variable inlet cowl.

Acknowledgments

The sponsorship by Dr. John Schmisseur and Dr. Fariba Fahroo of AFOSR is deeply appreciated. The fruitful and stimulating discussions with Dr. Donald Paul, Dr. Alan

Garscadden, Dr. Datta Gaitonde, and Dr. Roger Kimmel of AFRL, Dr. James Menart and Dr. P.G. Huang of Wright State University, as well as Dr. Sergey Surzhikov of the Russian Academy of Science are sincerely acknowledged.

References

[1] Murthy, S.N.B. and Curran, E.T., High speed flight propulsion systems, Progress in Aeronautics and Astronautics, AIAA, New York, 1991.
[2] Kurth, G., Critical physical phenomena in scramjet propulsion, AGARD-CP-600, 2002, pp. C5.1- C5.11.
[3] Bityurin, V., Kilmov, A., Leonov, S., Lutsky, A, Van Wie D., Brovkin, V., and Kolesnichenko, Yu., Effect of heterogeneous discharge plasma on shock wave structure and propagation, AIAA 99-4940, Norfolk VA, Nov. 1999.
[4] Leonov, S.B., Yarantsev, D.A., Gromov, V.G., and Kuriachy, A.P., Mechanisms of flow control by near-surface electrical discharge generation, AIAA 2005-0780, Reno NV, January 2005.
[5] Shneider, M.N. and Macheret, S.O., Hypersonic aerodynamic control and thrust vectoring by nonequilibrium cold-Air MHD devices, AIAA 2005-0979, Reno NV, January, 2005.
[6] Leonov, S., Bityurin, V., Savelkin, K., and Yarantsev, D., Effect of electrical discharge on separation processes and shock position in supersonic airflow, AIAA 2002-0355. Reno NV, January 2002.
[7] Bityurin, V.A., Bocharov, A.N., and Lineberry, J.T., Results of experiments on MHD hypersonic flow control, AIAA 2004-2263, Portland OR, June 2004.
[8] Shang, J.S. and Surzhikov, S.T., Magnetoaerodynamic actuator for hypersonic flow control, AIAA Journal Vol. 43, No. 8, August 2005, pp. 1633-1643.
[9] Shang, J.S. Surzhikov, S.T., Kimmel, R. Gaitonde, D.V., Hayes, J.R., and Menart, J., Mechanisms of plasma actuators for hypersonic flow control, Progress in Aerospace Sciences, Vol. 41, No. 8, Nov. 2005, pp.642-668.
[10] Updike, G., Shang, J.S., and Gaitonde, D.V., Hypersonic separated flow control using magneto-aerodynamic interaction, AIAA 2005-0164, Reno NV, January 2005.
[11] Poggie, J., Computational studies of high-speed flow control with weakly ionized plasma, AIAA 2005-0784, Reno NV, January 2005.
[12] Gaitonde, D.V., Simulation of local and global high-speed flow control with magnetic field, AIAA 2005-0560, Reno NV, January 2005.
[13] Borghi, C., Carraro, M., and Cristofolini, A., An axi-symmetric Hall configuration for the MHD interaction in hypersonic flows, AIAA 2005-4785, Toronto Canada, June 2005.
[14] Surzhikov, S.T., and Shang, J.S., The hypersonic quasineutral gas discharge plasma in a magnetic field, Proceedings of Third MIT Conference on Computational Fluid and Solid Mechanics, June 14-17, 2005, pp1004-1005.
[15] Raizer, Yu. P., Gas Discharge Physics, Springer-Verlag, Berlin, 1991.
[16] Mitchner, M. and Kruger, C.H. Jr. Partially ionized gases, John Wiley & Sons, 1973, pp.188-198.
[17] Sutton, G.W. and Sherman, A., Engineering Magnetohydrodynamics, McGraw-Hill, NY, 1965, pp.295-308.
[18] Shang, J.S., Electromagnetic perturbation to hypersonic viscous-inviscid interactions, AIAA 2006-0709, Reno NV, January 2006.
[19] Shang, J.S., Menart, J., Kimmel, R., and Hayes, J., Magneto-fluid-dynamics hypersonic compression inlet, AIAA 2006-0764, Reno NV, January 2006.

[20] Shang, J.S., Menart, J., Kimmel, R., and Hayes, J., Experimental investigation of magneto-fluid-dynamic compression in a cylindrical inlet, AIAA 2007-0399, Reno NV, January 2007.
[21] Surzhikov, S.T. and Shang, J.S. Two-component plasma model for two-dimensional glow discharge in magnetic field, J. Comput. Phys., Vol. 199, 2, Sept. 2004, pp. 437-464.
[22] Hayes, W.D., and Probstein, R.F., Hypersonic flow theory, Academy Press, 1959.
[23] Rumsey, C., Biedron, R., and Thomas, J., CFL3D: its history and some recent applications, NASA TM-112861, May 1997.
[24] Thomas, J.L., Diskin, B., Brandt, A., Textbook multigrid efficiency for fluid simulation, Annu. Rev. Fluid Mech., Vol. 35, January 2003, pp.317-340.
[25] Elisson, B. and Kogelschatz, U., Nonequilibrium volume plasma chemical processing, IEEE Trans. Plasma Science, Vol. 19, 1991, pp. 1063-77.
[26] Von Engel, A. and Steenbeck, M., Elektrische Gasenladungen, Vol. II, Springer, Berlin Germany, 1932.
[27] Hornung, H., Regular and Mach reflection of shock waves, Ann. Rev. Fluid Mech., Vol. 18, 1986, pp.33-58.
[28] M. S. Ivanov, G. N. Markelov, A. N. Kudryavtsev, and S. F. Gimelshein, Transition between regular and Mach reflection of shock waves in steady flow, AIAA-1997-2511, June 1997.
[29] Schlichting, H., Boundary-Layer Theory, 4^{th} edition, McGraw-Hill Inc., New York, 1960, p.190 & p.363.